Application of UV photoluminescence imaging spectroscopy for stacking faults identification on thick, lightly n-type doped, 4°-off 4H-SiC epilayers

AUTHOR(S):

Thierry-Jebali, N.; Kawahara, C.; Miyazawa, T.; Tsuchida, H.; Kimoto, T.

CITATION:

Thierry-Jebali, N. ...[et al]. Application of UV photoluminescence imaging spectroscopy for stacking faults identification on thick, lightly n-type doped, 4°-off 4H-SiC epilayers. AIP Advances 2015, 5(3)

ISSUE DATE:

2015-03-01

URL:

http://hdl.handle.net/2433/218243

Application of UV photoluminescence imaging spectroscopy for stacking faults identification on thick, lightly n-type doped, 4°-off 4H-SiC epilayers

N. Thierry-Jebali' , C. Kawahara, T. Miyazawa, H. Tsuchida, and T. Kimoto'

Citation: AIP Advances **5**, 037121 (2015); doi: 10.1063/1.4915128
View online: http://dx.doi.org/10.1063/1.4915128
View Table of Contents: http://aip.scitation.org/toc/adv/5/3
Published by the American Institute of Physics

AIP ADVANCES **5**, 037121 (2015)

Application of UV photoluminescence imaging spectroscopy for stacking faults identification on thick, lightly n-type doped, 4°-off 4H-SiC epilayers

N. Thierry-Jebali,[1,a] C. Kawahara,[1] T. Miyazawa,[2] H. Tsuchida,[2] and T. Kimoto[1,b]
[1]*Department of Electronic Science and Engineering, Kyoto University, Katsura, Nishikyo, Kyoto 615-8510, Japan*
[2]*Central Research Institute of Electric Power Industry (CRIEPI), 2-6-1 Nagasaka, Yokosuka, Kanagawa 240-0196, Japan*

(Received 2 February 2015; accepted 27 February 2015; published online 12 March 2015)

This paper deals with the description and the application of an original photoluminescence (PL) imaging technique on thick, lighly n-type doped 4H-SiC epilayers for in-grown stacking fault (SF) identification. This technique, call "photoluminescence imaging spectroscopy" (PLIS), compares different PL imaging pictures in order to create a new picture which displays the location and an approximation of the maximum photoemission wavelength of SFs at room temperature. Five types of SF have been detected and identified by PLIS on two different wafers. The origin of SF type modification during the growth is also discussed in this work. [http://dx.doi.org/10.1063/1.4915128]

I. INTRODUCTION

The excellent intrinsic properties of Silicon Carbide (SiC) as a wide band gap semiconductor make possible the development of the forthcoming electronic devices for high voltage, high temperature and high frequency applications.[1,2] For SiC power devices with a blocking voltage higher than 10 kilovolts, bipolar devices, such as PiN diodes, Bipolar Junction Transistors or thyristors are needed. Benefits on the on-state resistance are expected for bipolar devices owning to the effect of conductivity modulation.[3,4]

Despite the enthusiasm of developing very high voltage devices, the industrial development of SiC bipolar is facing some problems. One of these is the degradation of bipolar devices during operation.[5–7] Indeed, it has been observed that a forward bias on a *p-n* junction can induce the formation and motion of a single Shockley-type Stacking Fault (SF) through transformation of a Basal Plane Dislocation (BPD) in the voltage-blocking area. Since the different types of SF into 4H-SiC act as a quantum-well,[8] the generation of SF decreases the lifetime and consequently increases the differential resistance. This phenomenon is called "Forward Voltage Drift" (FVD).

To limit the FVD phenomenon, the key issue is to reduce the BPD density by an improvement of the 4H-SiC material quality. The reduction of BPD density is observed by decreasing the substrate off-cut angle.[9–11] A drastic reduction of the BPD density has been observed on epilayers grown on 4°-off substrates and a rather good material quality has been demonstrated for thick (> 120 μm) and n-type lightly doped (10^{14} cm^{-3} range) epilayers grown on 3-4 inch substrates.[12] However, the reduction of the off-cut angle generates another type of defects like 3C-inclusions[13] and in-grown SFs.[14–20]

One can see on Table I that the types of SFs are numerous (Single / Double / 8H Shockley SFs, Intrinsic / Multilayered / Extrinsic Frank-type SFs...).[16–19,21] These defects cause a reduction of

[a]nicolas.thierry-jebali@insa-lyon.fr
[b]kimoto@kuee.kyoto-u.ac.jp

TABLE I. PL emission wavelength of Franck-type and Shockley-type SFs for 4H-SiC. * This PL peak has been observed at 100 K.

SF type	Name	Notation	PL emission in nm at RT ($< 10\ K$)
Frank	Intrinsic	(5, 0)	488, (478, 485, 488, 490)[18]
	Multilayered	(4, 2)	457, (450, 455, 458, 460)[18]
	Extrinsic	(4, 1)	424, (415, 419, 423, 425)[18]
Shockley	Double SSF	(6, 2)	500[17]
	(3, 5) type	(5, 3)	480[16]
	8H-SiC	(4, 4)	467*, (463, 468, 472, 473)[21]
	8H-SiC	(4, 4)	?, (471, 477, 480, 482)[19]
	Single SSF	(3, 1)	420

the carrier lifetime and increase of the leakage current. Furthermore, the reduction of the substrate off-cut angle increases the expanding distance of the in-grown SFs (several mm for epilayer thickness $> 100\ \mu m$). The last point is a critical problem to reach a high processed devices yield. As a consequence, some specific solutions are needed in order to decrease the in-grown SFs density in thick epilayers.

At the beginning of any process improvement, there is the characterization of the nature and the location of in-grown SFs. Currently, many techniques are available for this purpose. Some of them are destructive like Transmission Electronic Microscopy (TEM) or KOH etching while some are non destructive like x-ray topography, micro-Photoluminescence mapping (PL mapping), Photoluminescence Imaging (PL imaging) or Cathodoluminescence (CL) imaging and spectroscopy. However, characterization techniques that display in a same picture, the location and the nature of SF are very limited. The common technique is to use a "real color" charge-coupled camera (CCD) on a PL or CL imaging characterization bench.[14,22,23]

This paper details a new PL characterization technique which localizes and identifies in-grown SFs. This technique is called Photoluminescence Imaging Spectroscopy (PLIS). The idea of PLIS is to make a spectroscopic picture of the sample from different UV-PL imaging pictures taken at different output filters (located before the CCD camera).

II. EXPERIMENTAL DETAILS

PLIS has been applied on two thick, lightly n-type doped epilayers (EPI1 & EPI2) grown on a 4°-off 3 inch substrate. The thickness and the doping concentration are $W_{EPI1} = 150\ \mu m$ and $N_{d-EPI1} = 2.6 \times 10^{14}\ cm^{-3}$ for EPI1 and $W_{EPI2} = 240\ \mu m$ and $N_{d-EPI2} = 1 \times 10^{14}\ cm^{-3}$ for EPI2. The growth conditions have been optimized in order to decrease the as-grown $Z_{1/2}$ concentration. As a result, a rather long effective carrier lifetime of $\tau_{EPI1} = 3 - 4\ \mu s$ and $\tau_{EPI2} = 8 - 9\ \mu s$ have been measured by microwave photoconductance decay for EPI1 and EPI2, respectively.

The PhotoLuminescence Imaging Spectroscopy technique is based on the conventional UV-PL imaging technique. In this study, the excitation source for samples was a Hg-Xe UV lamp filtered with a band-pass filter from $\lambda_{in} = 270\ nm$ to $\lambda_{in} = 380\ nm$. The UV lamp illuminated a $5 \times 8\ mm^2$ area with a power density of $0.9\ W \cdot cm^{-2}$. The PL imaging pictures have been collected with a deep depletion-type imaging CCD. The area of pictures was $660 \times 660\ \mu m^2$. Each picture has been filtered by a narrow (FWHM $< 10\ nm$) band-pass filter (output filter) at $420\ nm < \lambda_{out} < 500nm$. This output filter wavelength range corresponds to the bandwidth of all SFs photoemission in 4H-SiC (Table I).

In order to confirm the efficiency of PLIS for SF type recognition, PL spectroscopy at RT and 10 K has been used with a He-Cd ($\lambda = 325$ nm) laser as the excitation source.

III. DESCRIPTION OF THE PHOTOLUMINESCENCE IMAGING SPECTROSCOPY TECHNIQUE

The PLIS technique results on the collection and comparison of some UV-PL Imaging pictures taken at different output wavelengths (λ_{out}). The number of output filters is a trade-off between the

acquisition time and the resolution of the spectroscopic part of the PLIS picture. For this study, an output filter wavelength step of $\Delta\lambda_{out}$ of 10 nm has been used. So, the selected output filter wavelengths were [420, 430, 440, 450, 460, 470, 480, 490, 500] nm.

The procedure to obtain a PLIS picture is described as follows:

Step 1 Take PL imaging pictures of the sample for all selected output filter wavelengths. To make easier the comparison process, a constant acquisition time is better. In this study, the acquisition time was 1 s.

In order to illustrate the PLIS picture construction, a highly defected area from *EPI*1 with different types of in-grown SFs and some 3C-inclusions have been selected. Figure 1 reports the UV-PL imaging pictures of this area for different output filter wavelengths from 420 nm to 490 nm. One can see that some in-grown SFs are observable for only short output filter wavelengths (420, 430 nm) while others are better observed for longer wavelengths (460, 470, 480 nm). These initial observations demonstrate that different types of in-grown SFs are located in the same area. However, the identification of SF types is difficult in this stage.

Step 2 The efficiency of the CCD camera and the transmission rate of the optical filter depends on the wavelength. Since all PL Imaging pictures will be compared to each other in a next step, an

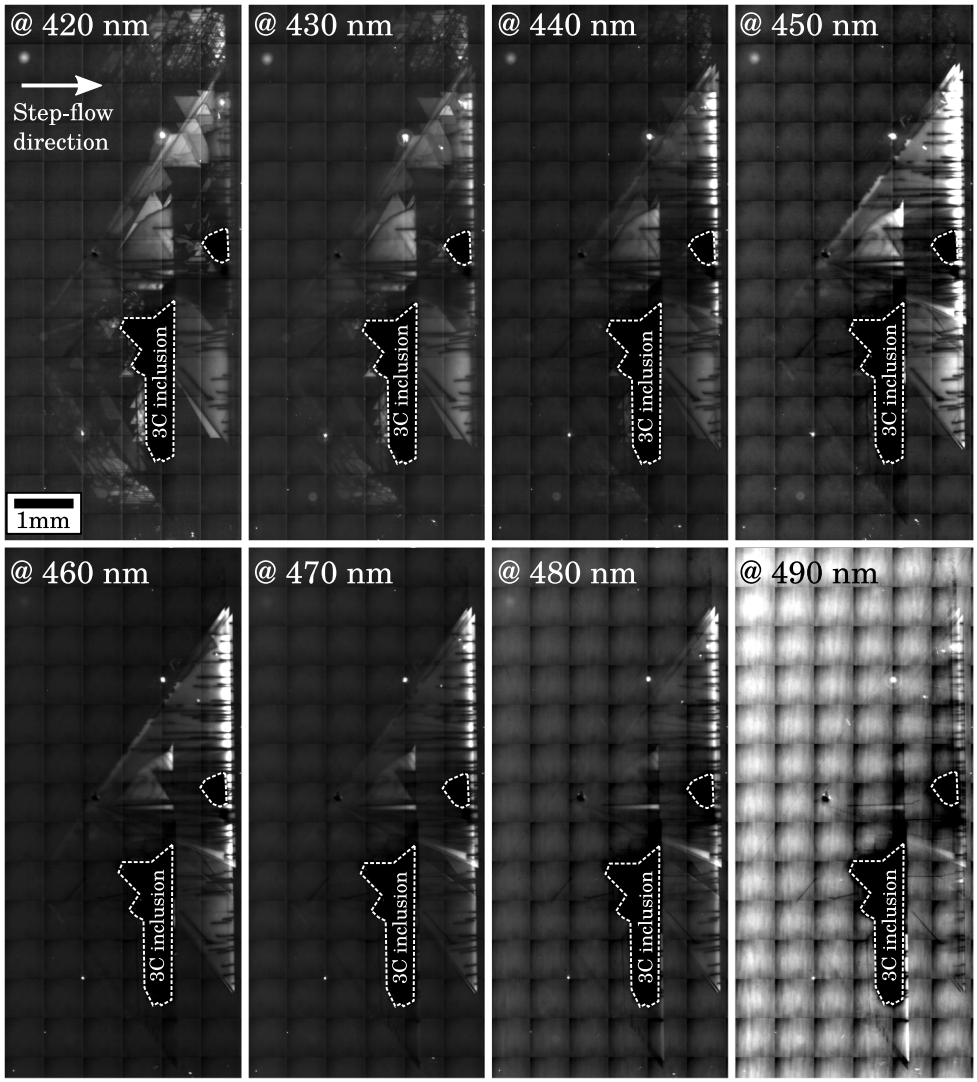

FIG. 1. UV-PL imaging pictures collected with differents output filter wavelengths from 420 nm to 490 nm of a highly defected area of EPI1 sample.

intensity correction factor must be applied to all pictures in order to take into account the system efficiency scattering.

Step 3 Then the 4H-SiC defect-free signal (background) is removed for all pictures. This step is important to guarantee that the observed signal is related to extended defects.

Step 4 This step compares all pictures together and builds new pictures at every output filter wavelengths. The pixel intensity of new pictures is set it up as follows: let consider $I_{\lambda 1}(x, y)$ as the pixel intensity of the PL imaging picture taken at wavelength λ1 and (x, y) the pixel coordinate. If $I_{\lambda 1}(x, y) > I_{\lambda - others}(x, y)$ then $Inew_{\lambda 1}(x, y) = I_{\lambda 1}(x, y)$ else $Inew_{\lambda 1}(x, y) = 0$, with $Inew$ the new picture pixel intensity and $\lambda - others$ the other output filter wavelengths. As a consequence, new pictures only contain maximum intensity pixels and give a good approximation of the maximum PL emission intensity wavelength of the defect.

Step 5 In order to make the final spectroscopic picture of the defect, the "gray scale" pictures are changed into "one color scale" pictures. A single color per output filter wavelength is applied (e.g. red for 460 nm, blue for 470 nm, etc...).

Figure 2 reports the transformation of UV-PL imaging pictures from Figure 1 after the comparison process and the modification of the "color scale." As observed earlier, the maximum intensity

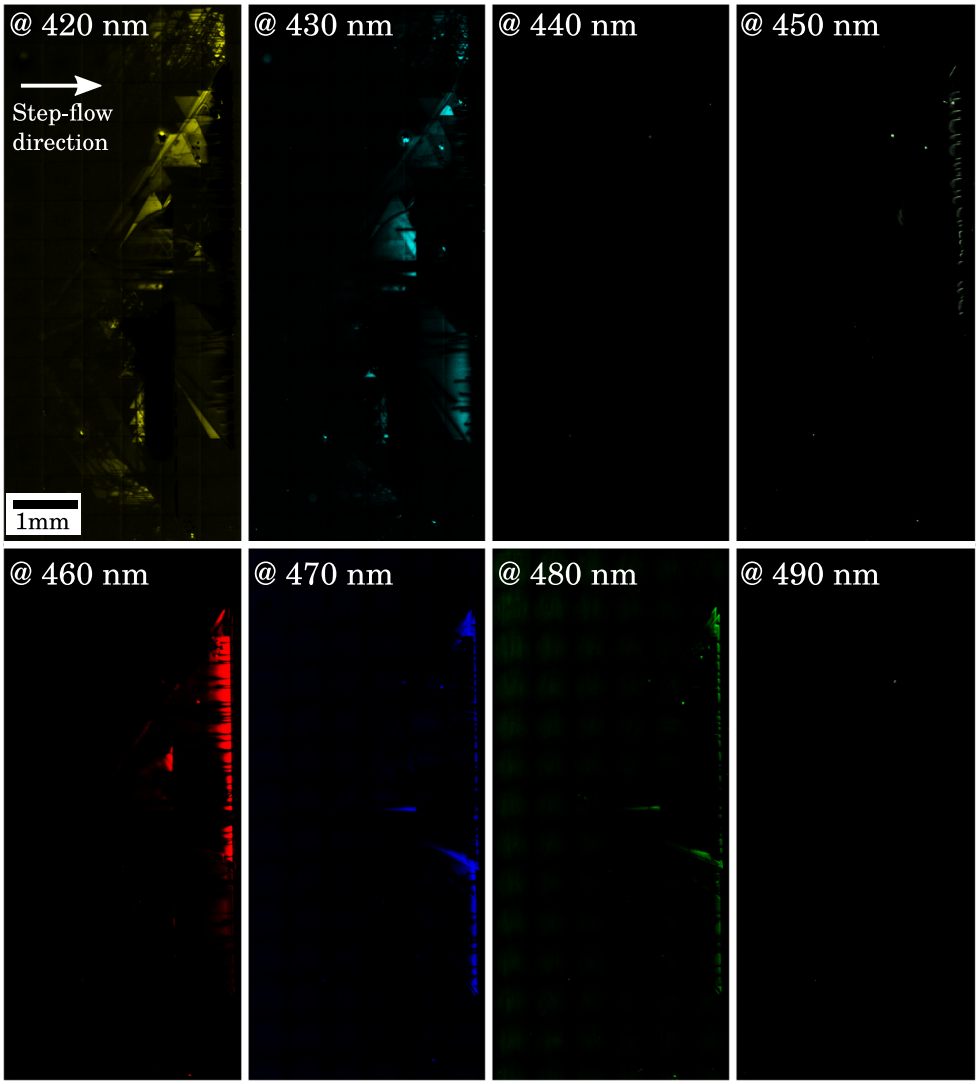

FIG. 2. Same UV-PL IMAGING pictures as FIG. 1 after the comparison process (step 4) and the modification of the "color scale" (step 5).

wavelength depends on the defect type but a better idea of the maximum photoemission intensity wavelength is given here with a good approximation of the maximum photoemission wavelength of the observed SFs.

Step 6 To get the final spectroscopic PL imaging picture, all pictures from "step 5" are added in a single picture. In order to make the PLIS picture understandable to everyone, the color legend is added on the picture.

Figure 3 reports two PLIS pictures examples build from figure 1 UV-PL imaging pictures. On figure 3(a), the different colors for wavelengths have been selected to make easier the discrimination of the different types of in-grown SF. By applying this configuration, four types of SF are easily observed. The maximum photoemission intensity wavelength are 420 nm, 430 nm and 460 nm for three types of SF and a mix of 470 nm and 480 nm wavelengths for the fourth one. This example clearly shows that PLIS technique is very useful to identify the different types of SF on highly defected areas.

Figure 3(b) shows a "real color" PLIS picture. For this configuration the selected colors correspond to the wavelength values. The four types of SF are also observed and yet the discrimination of different types of SF is more difficult, especially for wavelength varying from 460 nm to 480 nm. This is why the authors of this paper chose to use the figure 3(a) configuration.

IV. RESULTS AND DISCUSSIONS

A. Identification of in-grown of SFs by PLIS

Figure 4 exhibits PLIS pictures of the 5 types of SF detected in *EPI1* sample. The maximum photoemission intensity wavelength of observed SFs varies from 420 nm to 490 nm. Regarding the

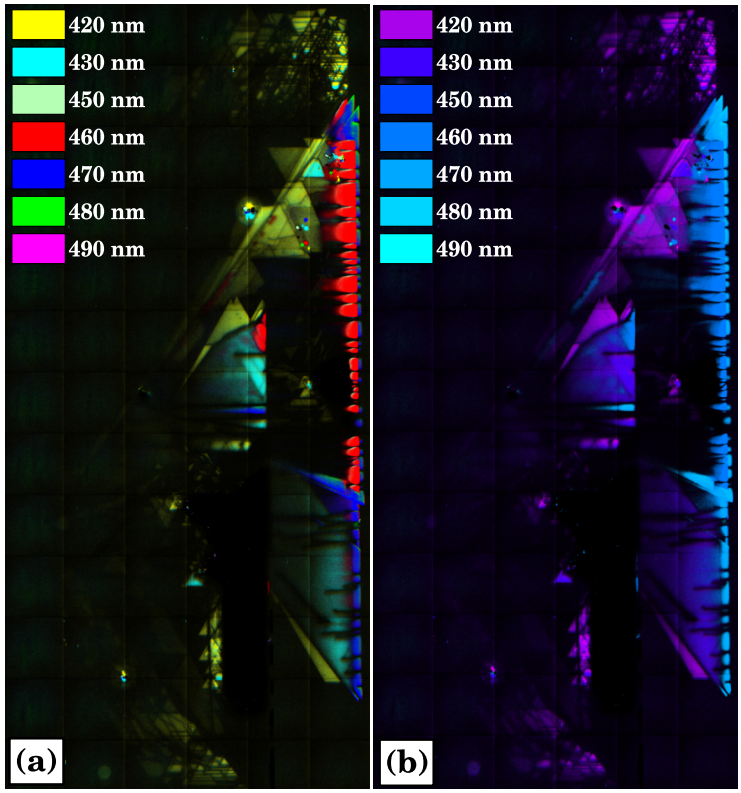

FIG. 3. PLIS pictures made from figure 1 UV-PL pictures. (a) The colors corresponding to the output filter wavelengths have been selected to make easier the discrimination of the different wavelengths. (b) Selected colors correspond to real color output filter wavelength.

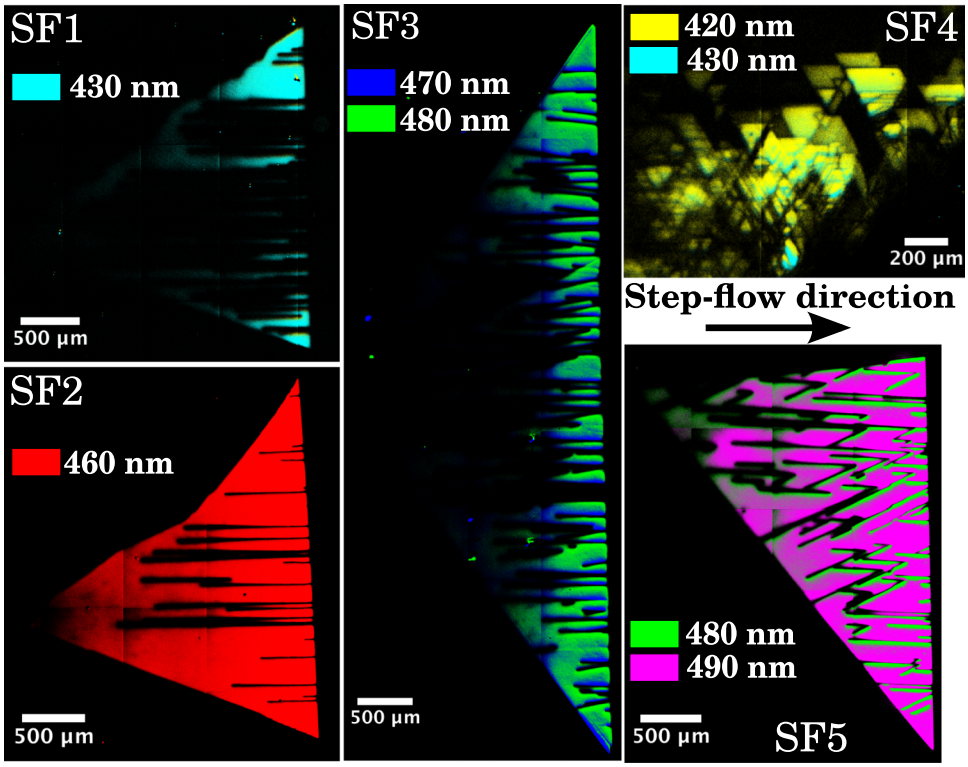

FIG. 4. PLIS pictures of 5 types of SFs from EPI1 sample.

SF expansion length (L_e), *SF1*, *SF2*, *SF3* and *SF5* defects nucleate at the epilayer/substrate interface ($L_e \approx 2.15\ mm \approx 150\ \mu m/tan\,(4°)$). In contrast, the scattering of L_e is high for SF4 type defect which means that this defect was formed in an advance state of the epilayer growth or at the initial stage of the the PL measurement. It is important to notice that the SF4 defect has only been detected close to 3C-inclusions where there is a high density of BPD.

Figure 5 reports PLIS pictures examples of *SF2*, *SF3* and *SF5* defects from *EPI2*. One can see an increase of the expanding distance to $L_e \approx 3.4\ mm \approx 240\ \mu m/tan\,(4°)$. Like *EPI1* sample, the formation of in-grown SF formation starts at the early stage of the epitaxial growth.

In order to confirm the effectiveness of PLIS technique, the approximation of the SF maximum photoemission wavelength obtained by PLIS has been compared to the maximum photoemission wavelength extracted from RT PL spectrum. Figure 6 displays the PL spectra at RT of *SF1*, *SF2*, *SF3*, *SF4* and *SF5* and Table II compares the maximum photoemission intensity wavelength (λ_{max}) extracted by PLIS and by PL spectroscopy.

A good agreement is observed for λ_{max} values extracted by PLIS and PL spectroscopy. The wavelength difference $\Delta\lambda_{max}$ is shorter than 4 nm for *SF1*, *SF2*, *SF4* and *SF5* which is the awaited value. These low $\Delta\lambda_{max}$ values is the consequence of the "only one" color of PLIS pictures.

The *SF3* PLIS picture is a combination of the λ_{out} = 470 nm and the λ_{out} = 480 nm UV-PL imaging pictures. This behavior can be explained by a larger PL peak of *SF3*. For example, if we compare *SF1* to *SF3*. The difference between the λ_{max} value extracted by PL spectroscopy and the closest output filter wavelength is similar and equal to 3 nm. Nevertheless, the full width at half maximum (FWHM) is equal to 23 nm and 36 nm for *SF1* and *SF3*, respectively. For *SF1*, the PLIS picture only contains signal from the UV-PL imaging picture taken at 430 nm while the *SF3* PLIS pictures contains signal from both 470 nm and 480 nm UV-PL imaging pictures. As a result, PLIS is a very useful characterization technique that provide a good approximation of the maximum photoemission intensity wavelength and some indications on the width of the corresponding PL spectrum peak.

Since PLIS technique has been validated by RT PL spectroscopy, some hypothesis can be formulated on the type of detected SF. From Table I, there are two types of SF for $420\ nm < \lambda_{max} < 430\ nm$.

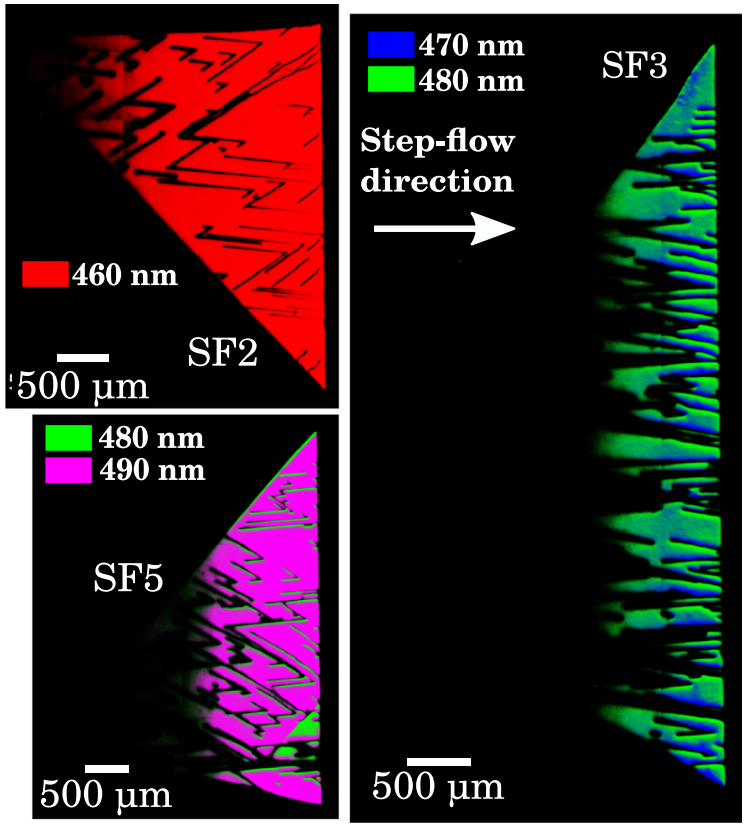

FIG. 5. PLIS pictures of SF2, SF3 and SF5 type defects from EPI2 sample.

Moreover, $\lambda_{max-SF4} < \lambda_{max-SF1}$ and *SF4* is exclusively located close to 3C-inclusion where the BPDs density is high. As a consequence, *SF4* should be a single Shockley SF and *SF1* an Extrinsic Franck-type SF. The maximum photoemission intensity wavelength of *SF5* agrees with an intrinsic Franck type SF.

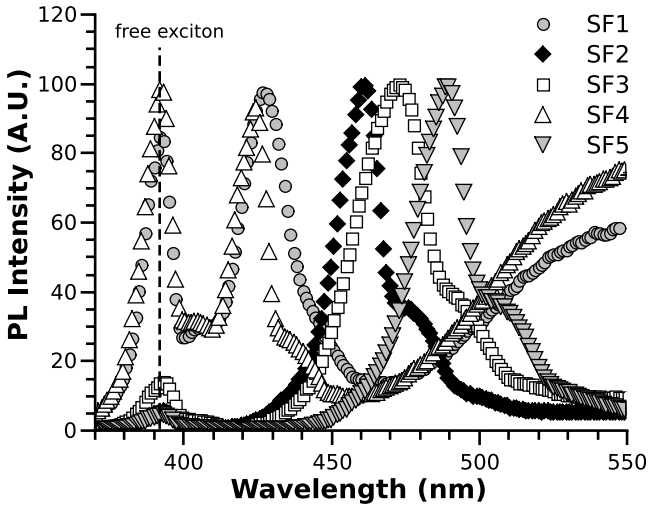

FIG. 6. PL spectra of SF1, SF2, SF3, SF4, SF5 collected at RT.

TABLE II. Comparison of the maximum photoemission intensity wavelength (λ_{max}) extracted by PLIS and by RT PL spectroscopy. FWHM is the full width at half maximum of the SF PL spectrum peak.

SF number	λ_{max} (nm) PLIS	λ_{max} (nm) PL spestroscopy	FWHM (nm)
SF1	430	427	23
SF2	460	461	19
SF3	$470 < \lambda_{max} < 480$	473	36
SF4	420	424	19
SF5	490	489	23

For *SF2* and *SF3*, the identification of the SF type from PLIS pictures is more complicated. On one hand, there are two types of SF for $\lambda_{max} \approx 460$ nm (multilayered Franck-type SF and 8H Shockley SF). So the identification of *SF2* cannot be done unambiguously. On the other hand, it does not exist to the best of our knowledge, any reported SF with $470\ nm < \lambda_{max} < 480\ nm$, while the 8H-SiC SF with 467 nm at 100 K observed by Izumi is a close example.[21] So the identification of *SF3* is impossible at this current state of investigation.

In order to identify the type of *SF2* and *SF3*, some PL spectra have been collected at $T = 10$ K. PL spectroscopy measurements have also been performed on *SF5* as a reference. The corresponding PL spectra are displayed on Figure 7. For *SF5* defects, the PL spectrum exhibits four sharp subpeaks at 479, 484.9, 488.2 and 490 nm and correspond to those already reported for an intrinsic Frank-type SF.[18]

The spectrum of *SF2* defect also shows four sharp subpeaks at 450.6, 455.6, 458.7 and 460 nm. The position of these peaks agrees with the peaks position of multilayered Frank-type SF.[18] On *EPI1* wafer, four *SF2* types defects have been observed. Three of these have been characterized by low temperature (LT) PL spectroscopy and exhibit similar behavior as the spectrum reported on Figure 7.

Finally, the position of the four subpeaks from SF3 LT PL spectrum at 471.6, 475.2, 479 and 480 nm agrees with the 8H-SiC Shockley-type SF LT PL spectrum reported by Marinova *et al.*[19] However, a final statement of the SF type for *SF3* is risky because a slightly higher LT PL peak energy has been reported by Izumi for the 8H-SiC SF.[21] Some TEM analyses are still under investigation to solve this problem.

Despite the risk of *SF3* identification, the authors make the hypothesis that *SF3* is a 8H-SiC SF for the next section of this paper.

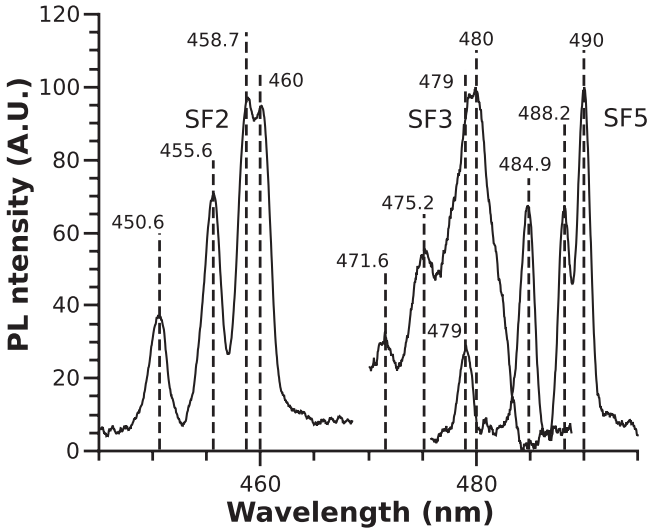

FIG. 7. PL spectra of SF2, SF3 and SF5 collected at $T = 10$ K.

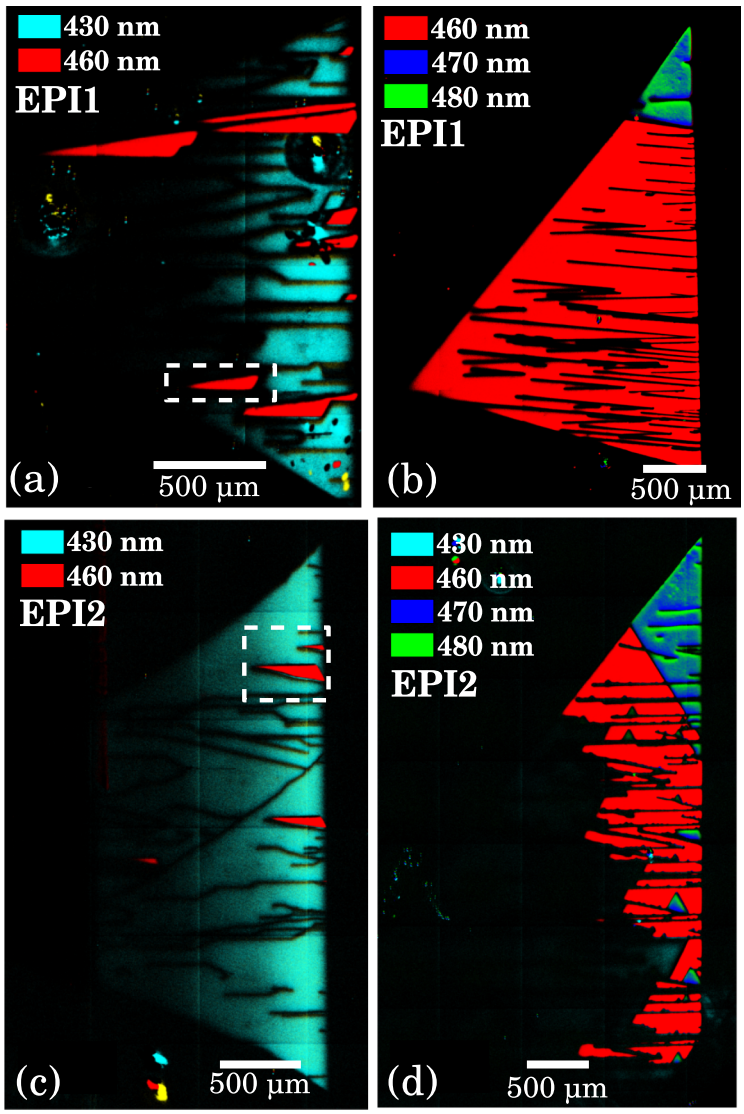

FIG. 8. Observation of SF type change during the growth from PLIS pictures. (a) Conversion of an extrinsic to a multilayered Frank type SF. The dashed rectangle corresponds to the area detailed on Figure 9(a)-9(b). (b) Conversion of a multilayered Frank-type SF to a 8H Shockley SF. (c) Conversion of an extrinsic to a multilayered Frank-type SF. The dashed rectangle corresponds to the area detailed on Figure 9(c). (d) Multiple SF conversion from extrinsic Frank-type SF to 8H Shokley SF.

B. Observation of the SF type modification by PLIS

By increasing the epilayer thickness, the probability of defects conversion also increases. For the case of in-grown SFs, the consequence can be a modification of the SF type during the growth.

Two types of SF modification have been observed by PLIS on *EPI1* and *EPI2* samples. The first one is the modification of an extrinsic to a multilayered Fank-type defect and the second one is the modification of a multilayered Frank-type SF to a 8H-SiC Shockley SF.

Tsuchida *et al.* reported the stacking sequence of Frank-type SFs.[24,25] All frank-type SF are confirmed to be created by four Frank partial dislocations (PD) (2 pairs) with a Burgers vector of 1/4[0001]. Frank type SF are formed by conversion of a *1c* threading screw dislocation (TSD) in the substrate as well as simultaneous generation of a *1c* TSD during epitaxial growth and by the insertion of loss of a single Si-C bilayer during epitaxial growth. The location of PDs in the crystal determine the nature of the SF. A single missing layer SF (or 3 extra layers SF) is an intrinsic SF. Then, a single

extra layer SF (or 3 missing layers SF) is an extrinsic SF. Finally, a two extra layers SF (or two missing layers SF) is a multilayered SF.

The conversion of an extrinsic to a multilayered Frank-type SF is observed on Figure 8(a) and 8(c). One can see on these PLIS pictures that the multilayered SFs are embedded in the main extrinsic SF with a triangular shape (or knife shape). Some of the multilayered SF enlarge along the basal plane up to the epilayer surface (see dashed rectangle on Figure 8(c)) while some are again converted onto extrinsic SF (see dashed rectangle on Figure 8(a)).

In order to understand the origin of the SF modification, PL imaging pictures have been acquired with a long pass filter (LPF) at $\lambda_{out} > 750\ nm$. This setup is convenient to observe and identify PD, BPD, threading screw dislocation (TSD) and threading edge dislocation (TED).[26,27]

Figure 9(a) exhibits the LPF PL imaging picture of the area bounded by a dashed rectangle on Figure 8(c) and illustrates the case of the multilayed SF enlargement up to the epilayer surface. Figure 9(b) is a superimposition of the PL imaging picture of Figure 9(a) and the PLIS picture of Figure 8(c). These pictures clearly show that a TSD is located at the origin of the multilayered SF where some new PDs are created.

Similar observations can be done for multilayered SF embedded in an extrinsic SF. Figure 9(c) is the superimposition of the dashed-line rectangle area of PLIS picture from Figure 8(a) and the corresponding LPF PL imaging picture. Like the previous case, a TSD (TDS 1 on Figure 9(c)) is located at the origin of the change of the extrinsic SF into a multilayered SF. In the same way, a TSD (TSD 2 on Figure 9(c)) is observed where a new modification of the SF type (multilayered to extrinsic SF) occurs.

The previous examinations tend to demonstrate that the modification of a Frank-type is related to the meeting of the SF with a TSD. This conclusion agrees with Tsuchida's paper[24] and is another clue of the SF type identification of *SF1* and *SF2* defects.

Pictures of Figure 10 are also a superimposition of the PLIS picture from Figure 8(d) and a LPF PL imaging picture of the same area. The observed SF is located close to a 3C-inclusion where a high dislocation density is detected. The signal from the LPF PL imaging picture of PDs indicates that only a small part of the SF type defect has been observed by PLIS. It means that another SF type conversion occurred during the growth. Unfortunately, the nature of the undetected part of the

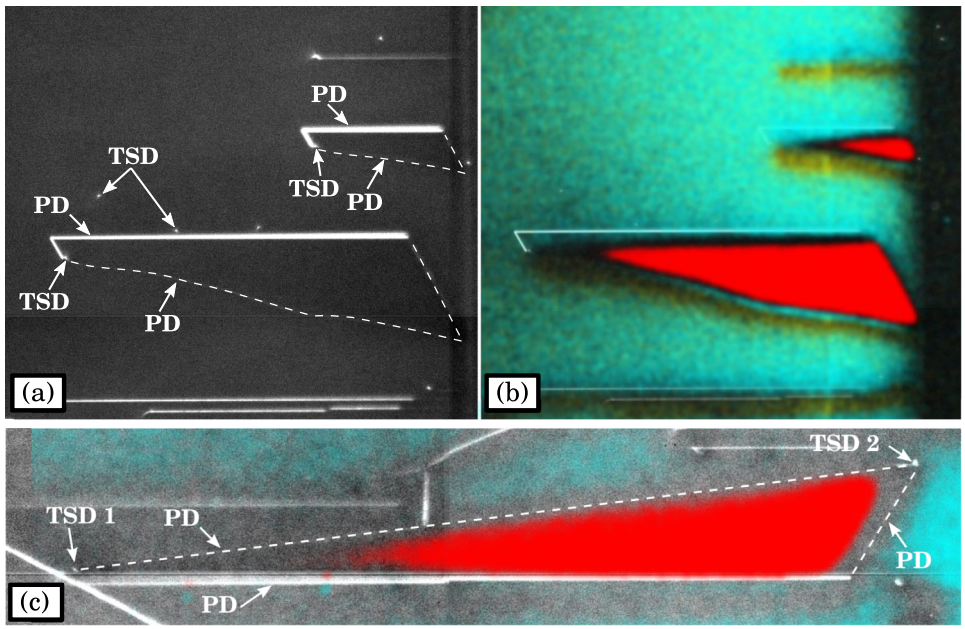

FIG. 9. (a) HPF PL imaging picture of the dashed rectangle area from Figure 8(c), (b) superimposition of the same HPF PL imaging picture with the corresponding PLIS pictures, (c) superimposition of the area bounded by a dashed rectangle from the PLIS picture of Figure 8(c) and the corresponding HPF PL imaging picture.

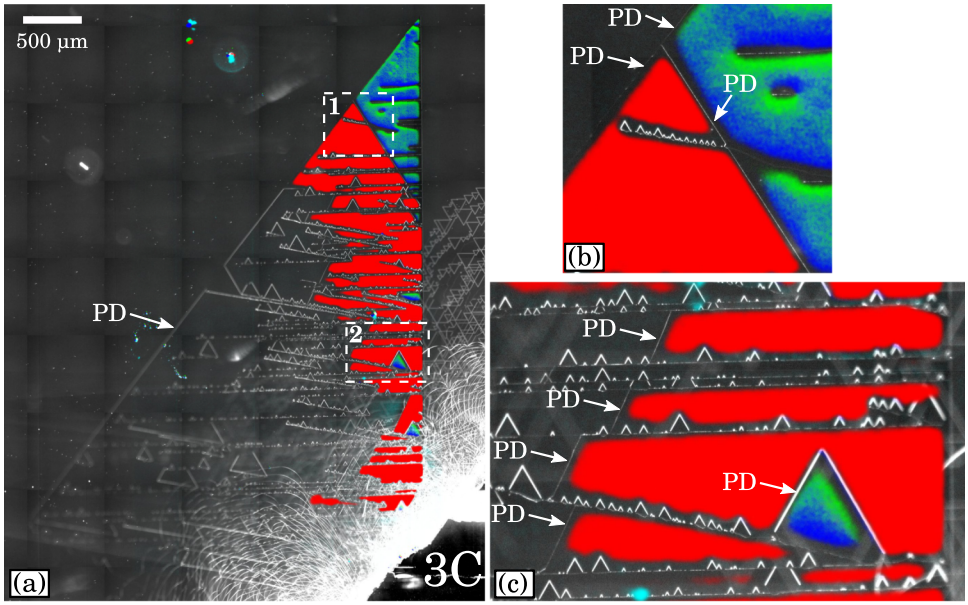

FIG. 10. Observation of SF type change during the growth. (a), (b) PLIS pictures from EPI1. (c) PLIS pictures from EPI2.

fault cannot be established unambiguously. In the same way, the change to a multilayered Frank fault is not clear. Figure 10(c) is a zoom of the dashed rectangle number 2 area of Figure 10(a) where a modification of the undefined SF to multilayered Frank fault is observed. One can see on this picture that there is a lot of PDs. Some of these bound multilayed Frank faults, some bound 8H inclusions but the nature or an approximation of the photoemission wavelength could not be detected by PLIS. The mechanism of SF conversion are also not clear but it is highly probable that the high stress induced by the 3C inclusion play a role on dislocation formation and fault type modification.

The change of multilayered Frank-type SF to 8H Shockley SF is well defined on the Figure 10(b) PLIS picture. Contrary to what has been observed for the extrinsic to multilayered SF change, there is no threading dislocation located at the origin of the SF type modification (see Figure 10(b)). It seems that this fault conversion is related to a pure epi-induced defect and agrees with the 8H Shockley SF identification in the previous section. Tsuchida *et al* made similar conclusions and identify two different ways to create 8H inclusion.[20] The first one is the overlapping of four Shockley faults (two double SFs) and the second is the overlapping of two Frank faults (intrinsic and extrinsic). Maybe, these two possibilities of 8H SF formation induce different photoemission properties and explain the variation in the PL spectra obtained by Izumi[21] and Marinova.[19]

V. CONCLUSION

In this study, we set it up an original PL imaging technique from the postulate that since the maximum PL intensity wavelength of in-grown SFs in 4H-SiC varies significantly from a SF to another one, the nature of the SF can be determine from an approximation of the maximum photoemission intensity wavelength at RT. Photoluminescence imaging spectroscopy technique is based on the comparison of different PL imaging pictures taken with a set of narrow band pass filters with different wavelengths located close to the CCD camera in order to extract an approximation of the maximum photoemission intensity wavelength. During the comparison process a new spectroscopic pictures of defects is created.

In conclusion this paper demonstrates that PLIS is useful for a fast recognition of the different types of in-grown SFs on thick and lightly n-type doped 4H-SiC epilayers and offers new prospects for systematic SFs detection and counting on a full wafer. Associated with other technique like PL

imaging or X-ray topography, PLIS is also helpful for understanding mechanisms of in-grown SF formation or modification.

ACKNOWLEDGMENT

This work was supported by the Funding Program for World-Leading Innovative R&D on Science and Technology (FIRST Program) from the Japan Society for the promotion of Science.

[1] H. Matsunami and T. Kimoto, "Step-controlled epitaxial growth of sic: High quality homoepitaxy," Materials Science and Engineering: R: Reports **20**, 125–166 (1997).
[2] M.-L. Locatelli and D. Planson, "Silicon carbide applications in power electronics," *Power Electronics Semiconductor Devices* (ISTE, 2010), pp. 185–265.
[3] H. Lendenmann, F. Dahlquist, J. Bergman, H. Bleichner, and C. Hallin, "High-power sic diodes: Characteristics, reliability and relation to material defects," *Materials Science Forum* (Trans Tech Publ, 2002), Vol. 389, pp. 1259–1264.
[4] J. Zhang, J. Zhao, P. Alexandrov, and T. Burke, "Demonstration of first 9.2 kv 4h-sic bipolar junction transistor," Electronics Letters **40**, 1381–1382 (2004).
[5] J. Bergman, H. Lendenmann, P. Nilsson, U. Lindefelt, and P. Skytt, "Crystal defects as source of anomalous forward voltage increase of 4h-sic diodes," *Materials Science Forum* (Trans Tech Publ, 2001), Vol. 353, pp. 299–302.
[6] H. Lendenmann, F. Dahlquist, N. Johansson, R. Söderholm, P. Nilsson, J. Bergman, and P. Skytt, "Long term operation of 4.5 kv pin and 2.5 kv jbs diodes," *Materials Science Forum* (Trans Tech Publ, 2001), Vol. 353, pp. 727–730.
[7] M. Skowronski and S. Ha, "Degradation of hexagonal silicon-carbide-based bipolar devices," Journal of Applied Physics **99**, 011101 (2006).
[8] S. Bai, G. Wagner, E. Shishkin, W. J. Choyke, R. P. Devaty, M. Zhang, P. Pirouz, and T. Kimoto, "Spectra associated with stacking faults in 4h-sic grown in a hot-wall cvd reactor," in *Materials Science Forum* (Trans Tech Publ, 2002), Vol. 389, pp. 589–592.
[9] J. Hassan, A. Henry, I. G. Ivanov, and J. P. Bergman, "In-grown stacking faults in 4h-sic epilayers grown on off-cut substrates," Journal of Applied Physics **105**, 123513 (2009).
[10] N. Thierry-Jebali, J. Hassan, M. Lazar, D. Planson, E. Bano, A. Henry, E. Janzén, and P. Brosselard, "Observation of the generation of stacking faults and active degradation measurements on off-axis and on-axis 4h-sic pin diodes," Applied Physics Letters **101**, 222111 (2012).
[11] J. Hassan, J. Bergman, A. Henry, and E. Janzén, "On-axis homoepitaxial growth on si-face 4h-sic substrates," Journal of Crystal Growth **310**, 4424–4429 (2008).
[12] T. Miyazawa and H. Tsuchida, "Thick 4h-sic epitaxial growth and defect reduction for very high voltage bipolar devices," ECS Journal of Solid State Science and Technology **2**, N3036–N3040 (2013).
[13] S. Leone, H. Pedersen, A. Henry, O. Kordina, and E. Janzén, "Improved morphology for epitaxial growth on 4° off-axis 4h-sic substrates," Journal of Crystal Growth **311**, 3265–3272 (2009).
[14] J. D. Caldwell, A. Giles, D. Lepage, D. Carrier, K. Moumanis, B. A. Hull, R. E. Stahlbush, R. L. Myers-Ward, J. J. Dubowski, and M. Verhaegen, "Experimental evidence for mobile luminescence center mobility on partial dislocations in 4h-sic using hyperspectral electroluminescence imaging," Applied Physics Letters **102**, 242109 (2013).
[15] J. Camassel and S. Juillaguet, "Optical properties of as-grown and process-induced stacking faults in 4h-sic," physica status solidi (b) **245**, 1337–1355 (2008).
[16] G. Feng, J. Suda, and T. Kimoto, "Triple shockley type stacking faults in 4h-sic epilayers," Applied Physics Letters **94**, 091910 (2009).
[17] G. Feng, J. Suda, and T. Kimoto, "Characterization of stacking faults in 4h-sic epilayers by room-temperature microphotoluminescence mapping," Applied Physics Letters **92**, 221906 (2008).
[18] I. Kamata, X. Zhang, and H. Tsuchida, "Photoluminescence of frank-type defects on the basal plane in 4h-sic epilayers," Applied Physics Letters **97**, 172107 (2010).
[19] M. Marinova, T. Robert, S. Juillaguet, I. Tsiaoussis, N. Frangis, E. Polychroniadis, J. Camassel, and T. Chassagne, "Combined structural and optical studies of stacking faults in 4h-sic layers grown by chemical vapour deposition," physica status solidi (a) **206**, 1924–1930 (2009).
[20] H. Tsuchida, I. Kamata, and M. Nagano, "Investigation of defect formation in 4h-sic epitaxial growth by x-ray topography and defect selective etching," Journal of Crystal Growth **306**, 254–261 (2007).
[21] S. Izumi, H. Tsuchida, I. Kamata, and T. Tawara, "Structural analysis and reduction of in-grown stacking faults in 4h-sic epilayers," Applied Physics Letters **86**, 202108 (2005).
[22] S. I. Maximenko, J. Freitas, P. B. Klein, A. Shrivastava, and T. Sudarshan, "Cathodoluminescence study of the properties of stacking faults in 4h-sic homoepitaxial layers," Applied Physics Letters **94**, 092101–092101–3 (2009).
[23] J. D. Caldwell, R. Stahlbush, and N. Mahadik, "Mitigating defects within silicon carbide epitaxy," Journal of The Electrochemical Society **159**, R46–R51 (2012).
[24] H. Tsuchida, I. Kamata, and M. Nagano, "Formation of basal plane frank-type faults in 4h-sic epitaxial growth," Journal of Crystal Growth **310**, 757–765 (2008).
[25] H. Tsuchida, M. Ito, I. Kamata, and M. Nagano, "Formation of extended defects in 4h-sic epitaxial growth and development of a fast growth technique," physica status solidi (b) **246**, 1553–1568 (2009).
[26] R. E. Stahlbush, N. A. Mahadik, and M. J. O'Loughlin, "Basal plane dislocations from inclusions in 4h-sic epitaxy," in *Materials Science Forum* (Trans Tech Publ, 2014), Vol. 778, pp. 309–312.
[27] M. Nagano, I. Kamata, and H. Tsuchida, "Photoluminescence imaging and discrimination of threading dislocations in 4h-sic epilayers," in *Materials Science Forum* (Trans Tech Publ, 2014), Vol. 778, pp. 313–318.